NJC

Accepted Manuscript

This is an *Accepted Manuscript*, which has been through the Royal Society of Chemistry peer review process and has been accepted for publication.

Accepted Manuscripts are published online shortly after acceptance, before technical editing, formatting and proof reading. Using this free service, authors can make their results available to the community, in citable form, before we publish the edited article. We will replace this *Accepted Manuscript* with the edited and formatted *Advance Article* as soon as it is available.

You can find more information about *Accepted Manuscripts* in the Information for Authors.

Please note that technical editing may introduce minor changes to the text and/or graphics, which may alter content. The journal's standard Terms & Conditions and the Ethical guidelines still apply. In no event shall the Royal Society of Chemistry be held responsible for any errors or omissions in this *Accepted Manuscript* or any consequences arising from the use of any information it contains.

ROYAL SOCIETY OF CHEMISTRY

www.rsc.org/njc

Cite this: DOI: 10.1039/c0xx00000x

www.rsc.org/xxxxxx

ARTICLE TYPE

Anion-assisted one-pot synthesis of 1D magnetic α- and β- MnO_2 nanostructures for recyclable water treatment application†

Pan-Yong Kuang[a], Min-Hua Liang[a], Wan-Yi Kong[a], Zhao-Qing Liu[a,*],Yun-Ping Guo[a], Hong-Juan Wang[a], Nan Li[a], Yu-Zhi Su[a], and Shuang Chen[b,*]

Received (in XXX, XXX) Xth XXXXXXXXX 20XX, Accepted Xth XXXXXXXXX 20XX
DOI: 10.1039/b000000x

Different crystal forms of MnO_2 exhibit not only diverse morphology and structure but also disparate performance. In view of this, we demonstrate a facile anion-assisted hydrothermal process to synthesize one-dimensional magnetic α- and β-MnO_2 nanostructures *via* altering the anions readily. The magnetic α- and β-MnO_2 nanostructures show excellent ability to remove organic pollutants compared to traditional adsorbents, which may be attributed to the crystal lattice oxygen and surface hydroxyl groups as well as the amount of surface Mn (□) and Mn (□). Furthermore, ease of recycle and the stability test proved that the β-MnO_2 is stable of performance for the degradation of methylene blue (MB), indicating the potential application in environment pollution purification.

1. Introduction

In the past decade, the design and fabrication of nanomaterials with specific structures, excellent performance, and defined composition have garnered numerous scientific and technological interests due to their intensive and wide applications in the catalysis,[1] supercapacitors,[2] adsorbents,[3] and photodetection,[4] *etc*. Recently, nanomaterials with different morphologies and polymorphs have been successfully synthesized, such as zero-dimensional (0D) nanoparticles, one-dimensional (1D) nanorods, nanowires, nanobelts and nanotubes, two-dimensional (2D) nanosheets and three-dimensional (3D) mesoporous nanostructures.[5-8] Among them, 1D nanomaterials have drawn the interests of many researchers owning to their unique chemical and physical properties such as large surface area and high aspect ratio,[9] high charge-discharge rates and short diffusion path lengths for ions.[10-12] Up to now, many researches and efforts have been directly put on the synthesis of 1D nanomaterials for multiple applications like solar cells,[13] optelectronics,[14] electromechanical nanoscale devices,[15] gas sensor devices,[16] photocatalysis,[17,18] and Li-ion batteries,[19] it has been aware of that 1D nanomaterials with well morphology, crystalline phase and performance is especially crucial for theoretical investigation and practical applications.[20,21]

As a typical transition-metal oxide, manganese oxide (MnO_2) has attracted considerable interests not only on account of its applications in electrochemical capacitor materials,[22] water treatment,[23] and catalyst,[24] but also its structural flexibility in space dimensions which can be prepared into different nanostructures. It is well-known that MnO_2 possess a huge structural flexibility and exists in a quantity of crystallographic forms, such as α-, β-, γ-, δ-, and ε-type, which depends on the ways [MnO_6] octahedral united.[25] Among them, α- and β-MnO_2 can be used as catalysts, absorbents, and electrode materials, *etc*.[26-28] γ-MnO_2 shows better electrical properties than commercial manganese dioxide in rechargeable Li-MnO_2 cells, it served as a promising and valuable candidate for cathode materials.[29] The physical and chemical properties of MnO_2 are significantly affected not only by the surface area, morphology and crystallographic structure, but also the synthetic route. To date, varieties of synthesis methods have been devoted to the preparation of MnO_2 nanostructures, for example, sol-gel pyrolysis,[30] refluxing methods,[31] and hydrothermal methods,[32] *etc*. However, most of these methods suffered from unavoidable disadvantages demanding harsh experimental conditions and/or complicated procedure, such as high temperature, high pressure, and long reaction time.

Herein, we present a feasible and facile synthetic route to fabricate one-dimensional α- and β-MnO_2 nanostructures with magnetic properties by anion-assisted method. It requires neither long time nor complex process or unique equipments. It is worth noting that the morphology and crystalline structure can be easily tuned by adjusting the different anions of raw materials. The magnetic α- and β-MnO_2 nanostructures show superior degradation properties compared to conventional adsorbents and can be recycled easily in water treatment application, which may be ascribed to the lattice oxygen and surface hydroxyl groups as well as the amount of surface Mn (□) and Mn (□). Moreover, the ease of recycle and high stability of β-MnO_2 in the degradation of MB dyes make it an alternative candidate for water treatment applications.

2. Experimental Section

2.1 Chemicals

All chemical reagents were analytical grade and were used directly without any further purification. Manganese acetate ($Mn(Ac)_2$•$4H_2O$), manganese sulphate ($MnSO_4$•H_2O), manganese chloride ($MnCl_2$•$4H_2O$), potassium permanganate ($KMnO_4$), Commercial manganese dioxide (MnO_2), active carbon, hydrogen peroxide (30% H_2O_2) and methylene blue (MB, $C_{16}H_{18}ClN_3S$) were all purchased from Sinopharm Chemical Reagent Co., Ltd (Shanghai, China).

2.2 Synthesis of 1D α- and β-MnO_2 Nanostructures

Analytical grade $Mn(Ac)_2$•$4H_2O$, $MnSO_4$•H_2O, $MnCl_2$•$4H_2O$ and $KMnO_4$ were used as received. In a typical procedure, 1.5 mmol $Mn(Ac)_2$•$4H_2O$ was dissolved in 20 mL distilled water to form a homogeneous and transparent solution with constant stirring. Then, 1.0 mmol $KMnO_4$ was added into the above solution, stirred for 30 min at room temperature to get a mixed solution. The solution was then subjected to hydrothermal treatment at 160 ℃ for 6 h in a stainless steel autoclave of 25 mL capacity with an inner Teflon liner. Upon completion of the reaction, the autoclave was cooled to room temperature and the precipitates were repeatedly washed with distilled water several times to remove the H^+ and other impurities. The products were then dried at 70 ℃ in air overnight. The sample was designated as M1 (α-MnO_2). For comparison, M2 (α-MnO_2) and M3 (β-MnO_2) were synthesised by substituted $MnSO_4$•H_2O and $MnCl_2$•$4H_2O$ for $Mn(Ac)_2$•$4H_2O$. The proposed chemical process between potassium permanganate and different manganese salts can be concluded as the following redox reactions and the synthesis process of α- and β-MnO_2 nanostructures was described as Scheme 1.

$$3Mn(Ac)_2 + 2KMnO_4 + 2H_2O \rightarrow 5\alpha\text{-}MnO_2 + 2KAc + 4HAc \quad (1)$$

$$3MnSO_4 + 2KMnO_4 + 2H_2O \rightarrow 5\alpha\text{-}MnO_2 + K_2SO_4 + 2H_2SO_4 \quad (2)$$

$$3MnCl_2 + 2KMnO_4 + 2H_2O \rightarrow 5\beta\text{-}MnO_2 + 2KCl + 4HCl \quad (3)$$

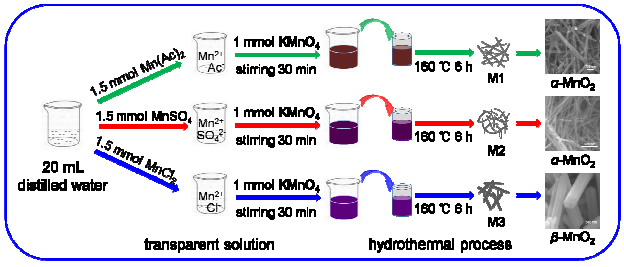

Scheme 1 Schematic representation of the synthesis process of α- and β-MnO_2.

2.3 Characterization

Powder X-ray diffraction (XRD) measurements were conducted on a PANalytical, PW3040/60 diffractometer with monochromatized Cu Kα radiation (λ = 0.15418 nm). The surface morphology of samples was examined using a scanning electron microscopy (SEM, JEOL JSM-7001F) equipped with an energy-dispersive spectroscopy (EDS) device and transmission electron microscopy (TEM, JEM2010-HR). Surface electronic states and compositions of the products were analyzed by X-ray photoelectron spectroscopy (XPS, ESCALab250). All binding energies were calibrated using the contaminant carbon (C 1s = 284.6 eV) as the reference, and Laser micro-Raman spectrometry (Renishaw inVia) was applied to record the Raman Spectra using a visible laser excitation of 514.5 nm at room temperature. The magnetic properties were studied by measuring hysteresis loops at low (5 K) and room temperature (300 K) using a quantum design MPMS-XL7 superconducting quantum interference device (SQUID) and a vibrating sample magnetometer (VSM) from Oxford Instruments, respectively. The Brunauer-Emmett-Teller (BET) specific surface area of the adsorbents was conducted on an ASAP 2020 instrument (USA).

2.4 Water treatment Experiments

In the experiments, the original solution was prepared by adding 20.0 mg of the as-prepared MnO_2 to 100.0 mL of 20.0 mg/L methylene blue (MB, a common cationic dye) aqueous solution under constant magnetic stirring at room temperature, then 2.0 mL H_2O_2 (30%) was added into the suspension. After a given time, about 5.0 mL of the suspension was taken for the following analysis after centrifugation, and the UV-vis spectrometer (UV, Shimadzu UV-3150) was used to measure the MB concentration remaining in the solutions. The changes of absorptions at 668 nm were applied to identify the concentrations of MB. In order to investigate whether the H_2O_2 play a primary role during the degradation process, that is, oxide and decompose the MB dyes or just a probe for the degradation, the experiment without adding the as-prepared MnO_2 was served as contrastive task.

3. Results and Discussion

3.1 XRD analysis

The phases of the MnO_2 samples were identified by XRD and the typical XRD patterns are presented in Fig. 1. For α-MnO_2 (M1 and M2), the products were synthesized by raw materials of $Mn(Ac)_2$•$4H_2O$ and $MnSO_4$•H_2O can be indexed to the tetragonal α-MnO_2 crystalline phase (JCPDS no. 44-0141) with lattice parameters a = 9.78 Å, b = 9.78 Å and c = 2.86 Å. For β-MnO_2 (M3), the product was synthesized by raw materials of $MnCl_2$•$4H_2O$ can be indexed to the tetragonal β-MnO_2 crystalline phase (JCPDS no. 24-0735) with lattice parameters a = 4.40 Å, b = 4.40 Å and c = 2.87 Å. All products exhibit a single phase since no peaks of any impurity phases could be detected from this pattern. Furthermore, the intense and sharp peaks indicate that the product is highly crystallized.

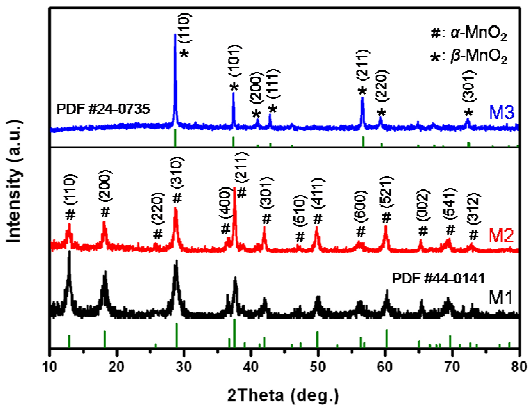

Fig. 1 XRD patterns of the as-synthesized magnetic MnO_2: M1 (α-MnO_2), M2 (α-MnO_2) and M3 (β-MnO_2).

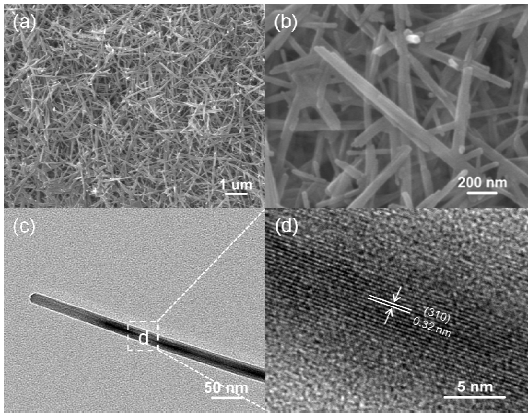

Fig. 2 (a,b) Panoramic and magnified SEM images, (c) TEM image, and (d) HRTEM image of α-MnO_2 (M1).

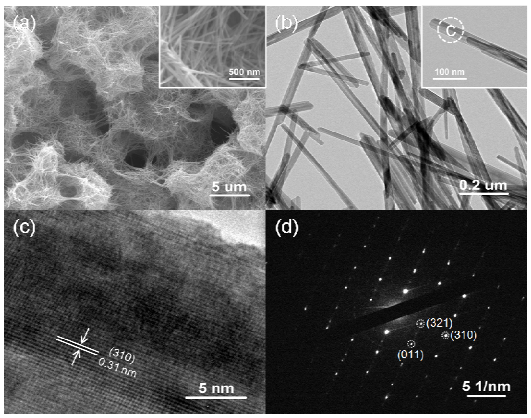

Fig. 3 (a) SEM image (inset is the higher magnification), (b) TEM images, (c) HRTEM image, and (d) SAED pattern of α-MnO_2 (M2).

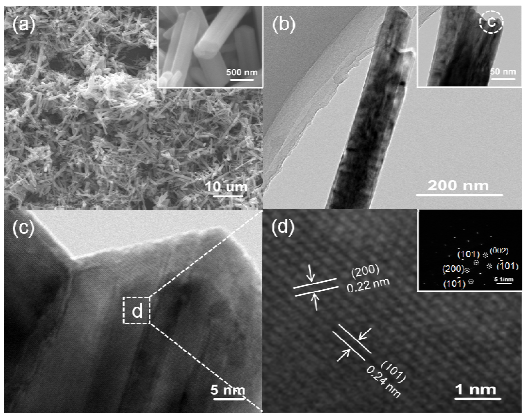

Fig. 4 (a) SEM image (inset is the higher magnification), (b) TEM images, (c,d) HRTEM images, and the inset is the corresponding SAED pattern of β-MnO_2 (M3).

3.2 Morphology and microstructure analysis

In order to examine the morphology and microstructure of the as-prepared α-MnO_2 (M1), scanning electron microscopy (SEM) and transmission electron microscopy (TEM) images are presented in Fig. 2. Panoramic and magnified SEM images (Fig. 2a-b) reveal the composition of uniform crossed 1D nanorods with average diameter of about 20 nm and length of several micrometers. Fig. 2c displays the TEM image of one α-MnO_2 nanorod, and Fig. 2d shows the corresponding high-resolution transmission electron microscopy (HRTEM) image to explore the crystallinity of the products. It can be obviously observed that the inter-planar distance of fringes parallel to the rod axis is 0.32 nm, which is consistent with the (310) plane of α-MnO_2.

The morphology and microstructure of the α-MnO_2 (M2) were also investigated. Compared with M1, M2 shows some changes in morphology even though their crystal forms are the same, which may be caused by different anions in manganese salts. Fig. 3a-b exhibits panoramic and magnified SEM images of M2. It can be clearly observed that the ultrathin nanowire with average diameter of about 40 nm and length of several micrometers intersected with each other to construct a nest-liked structure. The same results were also obtained in TEM characterization, as illustrated in Fig. 3b, the nanowires have diameters of about 40 nm, which matches the SEM analysis well. To further investigate the microstructure of the products, HRTEM and select area electron diffraction (SAED) patterns were provided in Fig. 3c-d. The apparent lattice spacing of about 0.31 nm between adjacent lattice agrees well in the inter-planar distance for (310) plane of α-MnO_2 and the corresponding SAED pattern suggests the single-crystalline nature of the nanowire.

Similar to the investigation of α-MnO_2, the analysis of microstructure was applied to β-MnO_2 (M3) and the morphology has obvious variation. The SEM image in Fig. 4a exhibits the smooth surface of the as-prepared nanogrooves. From the magnified SEM image (Fig. 4a, inset), it can be clearly observed that the nanogroove has two grooves on both sides of it. TEM and HRTEM images provide more information on the groove-like nanostructures. TEM images (Fig. 4b-c) reveal the nanogrooves have average diameters of about 100 nm, which is wider than those of M1 and M2. Fig. 4d gives the HRTEM image taken from a single nanogroove, the lattice spacing of 0.24 nm and 0.22 nm with the cross angle of about 60° are considered to be the (101) and (200) planes of β-MnO_2. Moreover, the SAED pattern in Fig. 4d indicates the nanogroove is a single crystal.

3.3 Raman spectroscopy analysis

Raman scattering spectroscopy is considered to be useful alternative and supplementary information to XRD for the characterizations of materials structure. Herein, Raman spectroscopy of the products was measured to analyze the local structure of MnO_2. As shown in Fig. 5, the Raman spectrum of α-MnO_2 (M1) shows four main peaks at 183, 385, 574, and 627 cm^{-1}, and three weak peaks at 330, 513, and 750 cm^{-1}.[33,34] By replacing the anion SO_4^{2-} with Ac^- ions resulted in α-MnO_2 (M2), the Raman spectrum shows four main peaks at 183, 385, 572, and 644 cm^{-1}, and three weak ones at 331, 518, and 756 cm^{-1} as well.[33,34] It is worth noting that all the α-MnO_2 type materials reported possess two diagnostic peaks at high-frequency region, about 574 and 634 cm^{-1},[35,36] the former bands are attributed to the M-O stretching vibration in the basal plane of [MnO_6] sheet, while the latter bands are related to the symmetric stretching vibration M-O of [MnO_6] groups.[37] For β-MnO_2 (M3), which was prepared by using anionic Cl^- anions, the Raman spectrum shows a sharp and intense peak at 654 cm^{-1}, which suggests that the rutile-structure has an interstitial space containing narrow one-dimensional (1×1) channels, the Raman band is acknowledged as the symmetric stretching vibration Mn-O of the

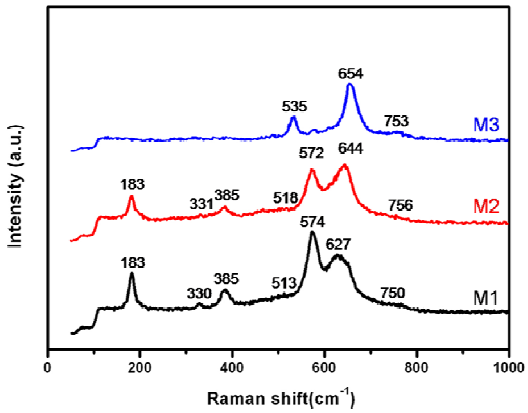

Fig. 5 (a) Raman spectra of M1 (α-MnO_2), M2 (α-MnO_2) and M3 (β-MnO_2), respectively.

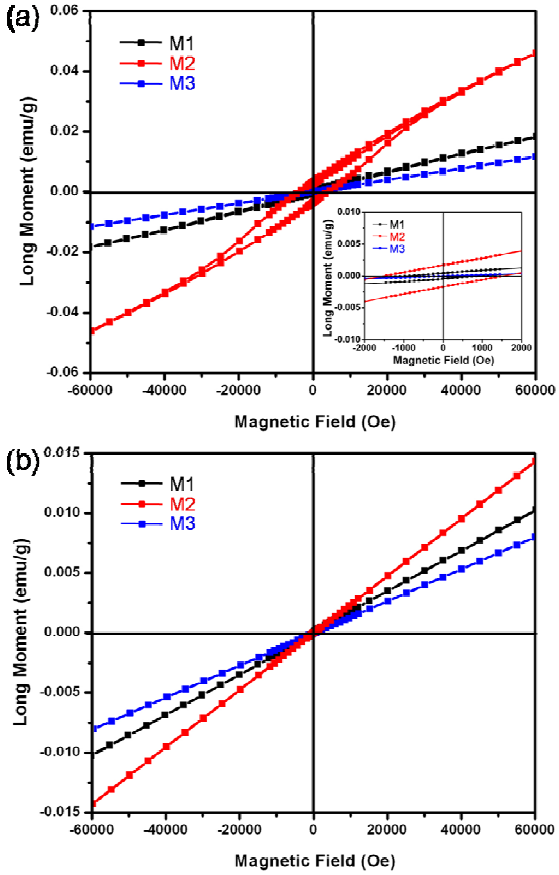

Fig. 6 (a) Low temperature 5 K hysteresis loops of M1, M2 and M3, and an enlarged view at low field is shown in the inset. (b) Room temperature hysteresis loops of M1 (α-MnO_2), M2 (α-MnO_2) and M3 (β-MnO_2).

[MnO_6] groups.[38] Meanwhile, two weak peaks at 753 and 535cm^{-1} are observed for β-MnO_2 which match fairly well to the previous reports.[39]

3.4 Magnetic properties investigation

Up to now, only a few studies reported the magnetic properties of MnO_2 nanostructures. The original ferromagnetism of the as-prepared MnO_2 was also investigated here. Fig. 6 shows the remnant magnetization versus applied coercivity field (M_r *vs* H_c) curves of the as-prepared MnO_2 acquired at two representative temperatures of 5 K and 300 K (inset: enlarged view at low fields). At 5 K, the coercivity field (H_c) of α-MnO_2 (M1 and M2) is 844.82 and 1555.36 Oe, and the corresponding remnant magnetization (M_r) is 4.48×10^{-4} and 1.69×10^{-3} emu/g, respectively. The hysteresis loop reveals a weak ferromagnetic behaviour at low temperature.[40] At 300 K, nearly linear M_r - H_c curves were observed for M1 and M2, indicating that a paramagnetic state exists in this temperature. The weak ferromagnetism of α-MnO_2 nanostructures at low temperature may be attributed to the charge separation of Mn^{4+} and Mn^{3+} and the different phenomena between the two temperatures are in agreement with previous reports that synthesized α-MnO_2 nanostructures through hydrothermal method.[41] As for β-MnO_2 (M3), no hysteresis loop at either 5 or 300 K was observed, indicating the magnetic state remains unchanged in the temperature range, the results reveal paramagnetic behaviour of the β-MnO_2, and there was not an anti-ferromagnetic transition in the temperature dependent experiment. From the above, the β-MnO_2 (M3) is easier to be recycled in practical application than M1 and M2, such as it can be absorbed from the solution by using magnet.

3.5 Degradation of MB solution

As is reported, transition metal oxides have been found to exhibit superior degradation properties for waste water treatment.[42,43] As a typical transition metal oxide, MnO_2 has attracted wide and enthusiastic focus due to its superior adsorptive properties in the application of water treatment for organic dyes. Herein, MB degradation experiments were performed to study the catalytic oxidation ability of the as-prepared α- and β-MnO_2 nanostructures by choosing H_2O_2 as an additive to induce a probe reaction.[44,45] As comparison trials, commercial MnO_2 and active carbon were selected to detect the remove capacity of MB species, respectively.[46,47] In addition, the adsorption experiments without introduction of H_2O_2 (as-prepared MnO_2 + MB) were conducted.

The degradation rates at different reaction time are shown in Fig. 7a. The degree of degradation was calculated by C_t/C_0, where C_t is the concentration of that at different intervals during the degradation and C_0 is the initial concentration of the MB solution. It could be seen that there is no change in the concentration of MB solution in absence of adsorbent, but obvious degradation occurred after adding the adsorbent. Moreover, the inset of Fig. 7a exhibits the adsorption efficiency of the experiments without introduction of H_2O_2 (as-prepared MnO_2 + MB), from which can be seen that the adsorption effect is negligible, indicating the adsorption is not the dominating process in the degradation of MB. As the reaction proceeded, the degradation rates of M1, M2 and M3 achieved at 75.40 %, 46.82 % and 93.24 % after 2.5 h, respectively. Remarkably, the as-prepared α- and β-MnO_2 have significant advantages in degradation ability compared with the traditional adsorbents commercial MnO_2 and active carbon in the purification of waste water. Furthermore, the as-prepared MnO_2 exhibits the similar or even higher degradation performances compared to some previous reports,[25,44,48] and it can be concluded that the adsorbents prepared in this work may serve as the candidate for the purification of sewage.

Furthermore, the reaction kinetics of the MB degradation

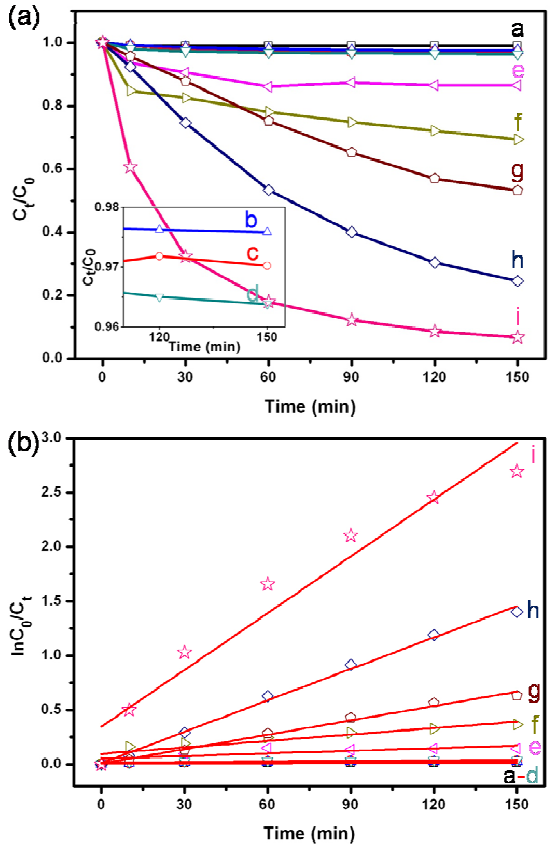

Fig. 7 (a) Degradation rates of MB (100 mL, 20 mg/L) on (a) MB + H_2O_2, (b) M2 (α-MnO_2) + MB, (c) M1 (α-MnO_2) + MB, (d) M3 (β-MnO_2) + MB, (e) commercial MnO_2 + MB + H_2O_2, (f) Active carbon + MB + H_2O_2, (g) M2 (α-MnO_2) + MB + H_2O_2, (h) M1 (α-MnO_2) + MB + H_2O_2 and (i) M3 (β-MnO_2) + MB + H_2O_2; And (b) plot of $\ln(C_0/C_t)$ versus degradation time.

were also investigated in Fig. 7b, the degradation data were analyzed with the pseudo-first-order model, $\ln(C_0/C_t) = kt$, where C_0 is the initial concentration of MB solution, C_t is the concentration of that at different intervals during the degradation, and k is the reaction rate constant (min^{-1}). The rate constants calculated from the data plotted were listed in Table S1†. It is very obvious that the MB degradation rate constant of β-MnO_2 (M3) is significantly higher than other adsorbents.

Fig. 8 shows the time-dependent degradation spectra of the MB solution degraded by the β-MnO_2 (M3), and the characteristic adsorption of MB at 615 nm and around 665 nm were selected for monitoring the degradation process. It is clearly observed that the three adsorption peaks vanished after 10 min of reaction time, and the intensity decrease gradually with the time elapse. Moreover, an evident blue shift took place for the characteristic peak, which implies the degradation of MB molecules and the possible formation of new species.[49]

3.6 Recycling stability test

It is well-known that the stability of the adsorbent during the degradation process is vitally important for its practical application. Herein, the β-MnO_2 (M3) was chose as a candidate for the examination of stability. Herein, the β-MnO_2 (M3) nanogrooves containing MB dye were collected by magnet and regenerated by combustion at 300 ℃ in air for 4 h. As shown in

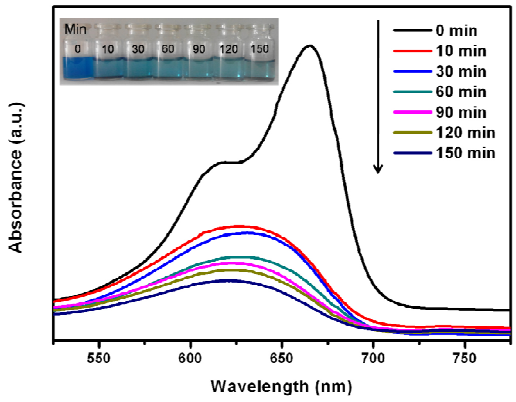

Fig. 8 Adsorption spectra of a solution of MB (100 mL, 20 mg/L) in the presence of β-MnO_2 (M3) at different intervals, the inset shows photos of degradation of MB with time by β-MnO_2 (M3).

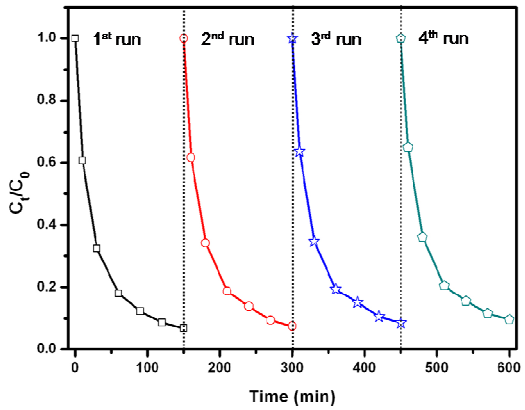

Fig. 9 Recycling test of the β-MnO_2 (M3) for degradation of MB solution.

Fig. 9, the recycled adsorbents could retain nearly the same degradation performance in the second, third and fourth circulations, which suggests that the β-MnO_2 (M3) is high stability and promising for practical application. In addition, the XRD pattern and SEM image after fourth circulation were provided in Fig. S1† and Fig. S2†, further demonstrating the stability in the degradation process.

3.7 The final products of degradation

To further confirm the decomposition of MB molecules and formation of other species, the ESI-MS analysis was conducted on the solution extracted from the system after 2.5 h, as presented in Fig. S3†. The peaks at m/z = 105 and 187 amu are corresponds to the *N*-methylene amine and 2H-benzo-[b][1,4]thiazin-7-amine, respectively. The peaks at m/z = 136 and 182 amu are corresponds to other smaller molecular fragments, which suggests the decomposition of the aromatic ring occurred on MB molecule.[49] Besides, there are no peaks for the intermediates such as azure B (270 amu), azure A (256 amu), azure C (242 amu) and thionin (228 amu) to be found, indicating the MB dye is completely degraded into small molecules.[50] The peak appearing at m/z = 316 amu demonstrates that two hydroxyl groups was coupled with the aromatic ring, indicating the residual MB in solution,[51] which can be verified by the degradation efficiency in Fig. 8 and the peak at m/z = 284 for methylene blue cations.

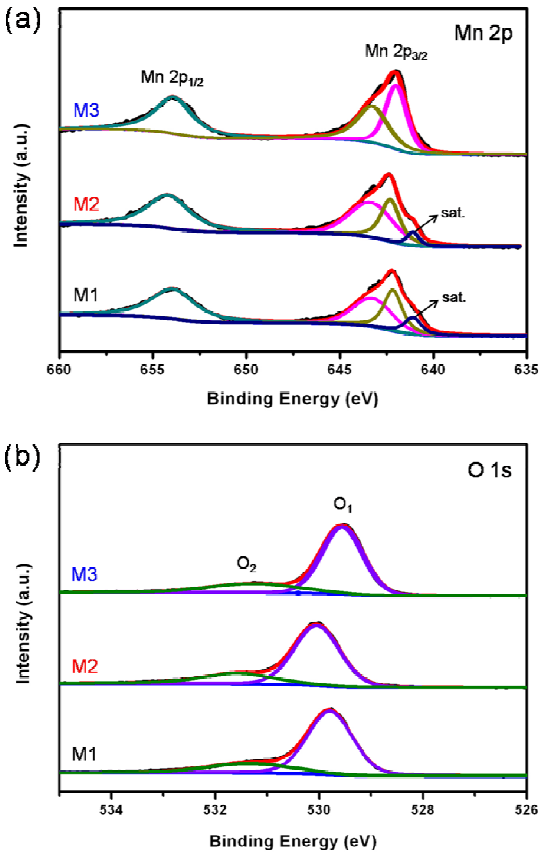

Fig. 10 (a) Mn 2p and (b) O 1s spectra of M1 (α-MnO_2), M2 (α-MnO_2) and M3 (β-MnO_2), respectively.

Table 1 Mn 2p and O 1s binding energies and related parameters

Adsorbents	Mn (Ⅲ)		Mn (Ⅳ)		Mn (sat.)	O_1		O_2	
	eV	%	eV	%	eV	eV	%	eV	%
M1 (α-MnO_2)	642.16	45.19	643.27	54.81	641.10	529.80	76.54	531.27	23.46
M2 (α-MnO_2)	642.32	39.02	643.35	60.98	641.11	530.05	75.88	531.56	24.12
M3 (β-MnO_2)	641.98	51.46	643.26	48.54	--	529.57	77.91	531.33	22.09

Mn (Ⅲ) (%, peak area) = Mn (Ⅲ)/[Mn (Ⅲ) + Mn (Ⅳ)] × 100.
Mn (Ⅳ) (%, peak area) = Mn (Ⅳ)/[Mn (Ⅲ) + Mn (Ⅳ)] × 100.
O_1 (%, peak area) = $O_1/(O_1 + O_2)$ × 100.
O_2 (%, peak area) = $O_2/(O_1 + O_2)$ × 100.

3.8 The effect factors of degradation efficiency

The different degradation efficiency among three adsorbents may be caused by the following aspects: the difference of XPS and isoelectric point. The typical X-ray photoelectron spectroscopy (XPS) survey spectra (in Fig. S4†) exhibits the products are composed of Mn, C and O elements, suggesting the formation of manganese dioxide. In general, the XPS spectrum of Mn $2p_{3/2}$can be divided into Mn (□), Mn (□) and sometimes includes a little satellite peak due to the small distinction between the binding energy values of Mn (□) and Mn (□).[52,53] According to the peak synthesis procedure, the peak splitting results and related parameters are presented in Fig. 10 and Table 1. The peaks at 641.98 ~ 642.32 eV and 643.26 ~ 643.35 eV were attributed to Mn (Ⅲ) and Mn (Ⅳ), respectively. The O 1s spectrum with two peaks centered at low binding energy (529.57 ~ 530.05) was assigned to the crystal lattice oxygen of [MnO_6] octahedral (denoted O_1), and the high binding energy (531.27 ~ 531.56) was ascribed to the adsorbed oxygen and surface hydroxyl groups (denoted O_2). The crystal lattice oxygen and surface hydroxyl groups as well as the amount of surface Mn (□) and Mn (□) play significant roles in the catalytic oxidation process.

Herein, MnO_2 adsorbs H_2O, H_2O_2 and MB molecules, it also transfer electrons between different state values. H_2O molecules were adsorbed on the surface of MnO_2 to produce surface hydroxyl groups. Subsequently, the surface hydroxyl groups decreased in the presence of cationic groups ($R\text{-}S^+$) of MB, which was caused by the electrostatic attraction. Electrons were transferred from the surface Mn (□) to H_2O_2 to create the free radical species, then to react with MB or recombine to form oxygen. Meanwhile, the Mn (□) converted to Mn (□) to maintain the electrostatic balance of MnO_2 in the reaction between H_2O_2 and MB, the obtained electrons of Mn (□) were transferred from the lattice oxygen thus inducing the generation of oxygen vacancies, which finally resulted in the increase of oxygen surface adsorption ability and accelerated the degradation of MB. Afterwards, the oxygen vacancies on the surface of MnO_2 were quickly and readily replenished by H_2O_2 in the system. In this adsorption and oxidation process, a cycling of Mn $(□)_{surf}$ → Mn $(Ⅳ)_{surf}$ → Mn $(Ⅲ)_{surf}$ was completed. Electrons from the surface Mn (Ⅲ) induced H_2O_2 to decompose to free radical species which led to the MB degradation, and the oxidation of lattice oxygen promoted the reversion of Mn (Ⅳ) to Mn (Ⅲ). From the above analysis, we can explain the different degradation efficiency for three adsorbents reasonably. β-MnO_2 (M3) has the maximum percentage composition of Mn (Ⅲ), which provide the maximum electrons for H_2O_2 to produce the free radical species to react with MB or recombine to form oxygen. At the same time, the maximum percentage composition of O_1 in β-MnO_2 (M3) provide the maximum electrons for Mn (□) to convert to Mn (□) to maintain the electrostatic balance and the maximum oxygen vacancies which finally resulted in the increase of oxygen surface adsorption ability and accelerated the degradation of MB. Therefore, the degradation efficiency for MB complied with the following orders: M3 (β-MnO_2) > M1 (α-MnO_2) > M2 (α-MnO_2).

Generally, MnO_2 in nearly neutral system (pH > pH_{zpc}) are abundant in hydroxyl groups on the surface,[54] which was also confirmed in our study. As showed in Fig. S5†, the pH of the zero point of charge of M1, M2 and M3 is 4.97, 5.43 and 4.81, respectively, and the pH of MB solution contained 2 mL H_2O_2 is about 7, indicating the negatively charged surface of the as-prepared MnO_2, which resulted in the effective adsorption of MB due to the electrostatic attraction. Furthermore, the M3 (β-MnO_2) has the smallest pH_{zpc} of 4.81, indicating the most hydroxyl groups on the surface and the highest adsorption efficiency. To confirm whether the specific surface area has played significant role in the degradation process, the Brunauer-Emmett-Teller (BET) specific surface area of the three adsorbents was investigated *via* N_2 adsorption-desorption test. As presented in Fig. S6†, the BET specific surface area of M1, M2 and M3 was

calculated to be 29.82, 29.57 and 3.88 m^2/g, respectively. It is dramatic that the β-MnO_2 (M3) displays the highest degradation efficiency while exhibits the smallest specific surface area, the M1 and M3 show different degradation efficiency but have the similar specific surface area. Therefore, the results definitely revealed that the specific surface area has the negligible influence in the degradation process, and the degradation efficiency could be mainly attributed to the oxygen vacancies and surface hydroxyl groups as well as the amount of surface Mn (□) and Mn (□) in the process.

3.9 The possible mechanism of degradation

The possible degradation mechanism was presented. As the results shown in Fig. 7a, it can be seen that when H_2O_2 was added individually to the MB solution, there is no decrease of the concentration of MB, indicating that no degradation occurred. Since the MnO_2 and H_2O_2 were mixed together in the MB solution, apparent degradation of MB took place, especially for β-MnO_2 (M3), which was consistent with the previous report.[48,55] According to the work of Yu *et al.*[56], the degradation mechanism can be elucidated as four steps, as described in Fig. 11. H_2O_2 was adsorbed on the surface of the MnO_2 (step 1). Subsequently, the H_2O_2 was decomposed into free radical species, such as $\bullet HO_2$, $\bullet O_2^-$ *et al.* (step 2). Adsorbed dyes were mineralized to form CO_2, H_2O or other small species owning to high oxidative ability of the free radical species (step 3). This is a pathway that free radical species are consumed, another is that the free radical species recombination to form O_2 (step 4), but the O_2 is unable to oxide the dye molecules, which was proven in our experiments because there are oxygen produced and the concentration of MB solution retained invariable in absence of adsorbents. On the contrary, lots of oxygen produced and the concentration of MB solution decreased acutely in the presence of adsorbents. In the end, the produced small species released from the surface of the adsorbent thus to make it reutilized, which matches well with the results of the stability test.

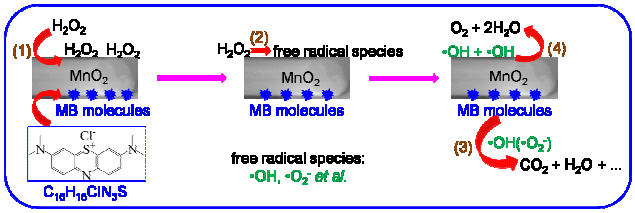

Fig. 11 Proposed mechanism of β-MnO_2 (M3) in the degradation process of MB dyes in the presence of H_2O_2.

Conclusions

In summary, one-dimensional α- and β-MnO_2 nanostructures with highly crystallized and magnetic properties have been successfully synthesized through a novel hydrothermal approach with different manganese salts. The magnetic α- and β-MnO_2 show superior degradation performance compared to traditional adsorbents, which may be attributed to the lattice oxygen and surface hydroxyl groups as well as the amount of surface Mn (□) and Mn (□). In addition, ease of recycle and high stability in water treatment for removing organic pollutants of the as-prepared β-MnO_2 demonstrates the promising application in environment pollution treatment.

Acknowledgements

This work was supported by Natural Science Foundations of China (Grant No. 21306030 and 21203036), Guangdong Natural Science Foundation (Grant No. s2012010009719 and s2013040015229), Program Foundation of the second batch of innovation teams of Guangzhou Bureau of Education (Grant No. 13C04), Scientific Research Project of Guangzhou Municipal Colleges and Universities (Grant No. 2012A064), and the Fresh Talent Program of Guangzhou University (Grant No. 201302).

Notes and references

[a]*School of Chemistry and Chemical Engineering/Guangzhou Key Laboratory for Environmentally Functional Materials and Technology Guangzhou University; Guangzhou Higher Education Mega Center, Waihuan Xi Road No. 230, China 510006 Fax: 86-20-39366908; Tel: 86-20-39366908; E-mail:lzqgzu@gzhu.edu.cn*
b Guangzhou institute of railway technology, Guangzhou 510430, China E-mail:drschen@126.com

1 Y. M. Li and G. A. Somorjai, *Nano Lett.*, 2010, **10**, 2289-2295.
2 W. F. Wei, X. W. Cui, W. X. Chen and D. G. Lvey, *Chem. Soc. Rev.*, 2011, **40**, 1697-1721.
3 M. M. Khin, A. S. Nair, V. J. Babu, R. Murugan and S. Ramakrishna, *Energy Environ. Sci.*, 2012, **5**, 8075-8109.
4 T. Y. Zhai, L. Li, Y. Ma, M. Y. Liao, X. Wang, X. S. Fang, J. N. Yao, Y. Bando and D. Golberg, *Chem. Soc. Rev.*, 2011, **40**, 2986-3004.
5 J. B. Fei, Y. Cui, X. H. Yan, W. Qi, Y. Yang, K. W. Wang, Q. He and J. B. Li, *Adv. Mater.*, 2008, **20**, 452-456.
6 K. Pan, Y. Z. Dong, W. Zhou, Q. J. Pan, Y. Xie, T. F. Xie, G. H. Tian and G. F. Wang, *ACS Appl. Mater. Interfaces*, 2013, **5**, 8314-8320.
7 Y. C. Qiu, K. Y. Yan, H. Deng and S. H. Yang, *Nano Lett*., 2012, **12**, 407-413.
8 Z. Y. Liu, Q. Q. Zhang, T. Y. Zhao, J. Zhai and L. Jiang, *J. Mater. Chem.*, 2011, **21**, 10354-10358.
9 B. Nikoobakht, X. D. Wang, A. Herzing and J. Shi, *Chem. Soc. Rev.*, 2013, **42**, 342-365.
10 N. Li, J. Y. Wang, Z. Q. Liu, Y. P. Guo, D. Y. Wang, Y. Z. Su and S. Chen, *RSC Adv.*, 2014, **4**, 17274-17281.
11 G. Q. Zhang, H. B. Wu, H. E. Hoster, M. B. Chan-Park and X. W. Lou, *Energy Environ. Sci.*, 2012, **5**, 9453-9456.
12 W. B. Yan, J. Y. Kim, W. D. Xing, K. C. Donavan, T. Ayvazian and R. M. Penner, *Chem. Mater.*, 2012, **24**, 2382-2390.
13 L. Wang, H. Q. Liu, R. M. Konik, J. A. Misewich and S. S. Wong, *Chem. Soc. Rev.*, 2013, **42**, 8134-8156.
14 H. Q. Li, X. Wang, J. Q. Xu, Q. Zhang, Y. S. Bando, D. Golberg, Y. Ma and T. Y. Zhai, *Adv. Mater.*, 2013, **25**, 3017-3037.
15 S. I. Cho and S. B. Lee, *Acc. Chem. Res.*, 2008, **41**, 699-707.
16 G. Z. Shen, P. C. Chen, K. M. Ryu and C. W. Zhou, *J. Mater. Chem.*, 2009, **19**, 828-839.
17 O. Eder, *Chem. Rev.*, 2010, **110**, 1348-1385.
18 K. F. Wu, H. M. Zhu, Z. Liu, W. R. Córdoba and T. Q. Lian, *J. Am. Chem. Soc.*, 2012, **134**, 10337-10340.
19 H. W. Lee, P. Muralidharan, R. Ruffo, C. M. Mari, Y. Cui and D. K. Kim, *Nano Lett.*, 2010, **10**, 3852-3856.
20 J. Y. Yuan, Y. Y. Xu and A. H. E. Müller, *Chem. Soc. Rev.*, 2011, **40**, 640-655.
21 Y. S. Zhao, H. B. Fu, A. D. Peng, Y. Ma, Q. Liao and J. N. Yao, *Acc. Chem. Res.*, 2010, **43**, 409-418.
22 K. Xiao, J.-W. Li, G.-F. Chen, Z.-Q. Liu, N. Li, Y.-Z. Su, *Electrochim. Acta*, 2014, **149**, 341-348.
23 S. Jeon and K. Yong, *J. Mater. Chem.*, 2010, **20**, 10146-10151.
24 F. Jiao and F. Hrei, *Energy Environ. Sci.*, 2010, **3**, 1018-1027.

25 F. Li, J. F. Wu, Q. H. Qin, Z. Li and X. T. Huang, *J. Alloys Compd.*, 2010, **492**, 339-346.
26 V. B. R. Boppana and F. Jiao, *Chem. Commun.*, 2011, **47**, 8973-8975.
27 J. Cao, Q. H. Mao, L. Shi and Y. T. Qian, *J. Mater. Chem.*, 2011, **21**, 16210-16215.
28 D. W. Su, H. J. Ahn and G. X. Wang, *J. Mater. Chem. A*, 2013, **1**, 4845-4850.
29 J. H. Zeng, Y. F. Wang, Y. Yang and J. Zhang, *J. Mater. Chem.*, 2010, **20**, 10915-10918.
30 S. F. Chin, S. C. Pang and M. A. Anderson, *Mater. Lett.*, 2010, **64**, 2670-2672.
31 A. K. Sinha, M. Pradhan and T. Pal, *J. Phys. Chem. C*, 2013, **117**, 23976-23986.
32 X. H. Duan, J. Q. Yang, H. Y. Gao, J. M. Ma, L. F. Jiao and W. J. Zheng, *CrystEngComm*, 2012, **14**, 4196-4204.
33 T. Gao, M. Glerup, F. Krumeich, R. Nesper, H. Fjellvåg and P. Norby, J. *Phys. Chem. C*, 2008, **112**, 13134-13140.
34 T. Gao, H. Fjellvåg and P. Norby, *Anal. Chim. Acta*, 2009, **648**, 235-239.
35 M. D. Wei, Y. Konishi, H. S. Zhou, H. Sugihara and H. Arakawa, *Nanotechnology*, 2005, **16**, 245.
36 M. Polverejan, J. C. Villegas and S. L. Suib, *J. Am. Chem. Soc.*, 2004, **126**, 7774-7775.
37 Z. B. Lei, J. T. Zhang and X. S. Zhao, *J. Mater. Chem.*, 2012, **22**, 153-160.
38 S. B. Ma, K. Y. Ahn, E. S. Lee, K. H. Oh and K. B. Kim, *Carbon*, 2007, **45**, 375-382.
39 T. Gao, H. Fjellvåg and P. Norby, *Nanotechnology*, 2009, **20**, 055610.
40 J. G. Zhao, J. Z. Yin and S. G. Yang, *Materials Research Bulletin*, 2012, **47**, 896-900.
41 J. Luo, H. T. Zhu, J. K. Liang, G. H. Rao, J. B. Li and Z. M. Du, *J. Phys. Chem. C*, 2010, **114**, 8782-8786.
42 J. Cao, Q. H. Mao, L. Shi and Y. T. Qian, *J. Mater. Chem.*, 2011, **21**, 16210-16215.
43 J. Wang, J. Liu and Y. C. Zhou, *RSC Adv.*, 2013, **3**, 25937-25943.
44 J. L. Zhou, L. Yu, M. Sun, B. Lan, F. Ye, J. He and Q. Yu, *Mater. Lett.*, 2012, **79**, 288-291.
45 Z. C. Bai, B. Sun, N. Fan, Z. C. Ju, M. H. Li, L. Q. Xu and Y. T. Qian, *Chem. Eur. J.*, 2012, **18**, 5319- 5324.
46 R. X. Chen, J. G. Yu and W. Xiao, *J. Mater. Chem. A*, 2013, **1**, 11682-11690.
47 J. Cao, Q. H. Mao, L. Shi and Y. T. Qian, *J. Mater. Chem.*, 2011, **21**, 16210-16215.
48 H. J. Cui, H. Z. Huang, M. L. Fu, B. L. Yuan and W. Pearl, *Catal. Commun.*, 2011, **12**, 1339-1343.
49 G. X. Zhao, J. X. Li, X. M. Ren, J. Hu, W. P. Hu and X. K. Wang, *RSC Adv.*, 2013, **3**, 12909-12914.
50 M. Zaied, S. Peulon, N. Bellakhal, B. Desmazieres and A. Chausse, *Appl. Catal. B*, 2011, **101**, 441-450.
51 T. Sriskandakumar, N. Opembe, C. H. Chen, A. Morey, C. King and S. L. Suib, *J. Phys. Chem. A*, 2009, **113**, 1523-1530.
52 Y. Dai, X. Y. Wang, Q. G. Dai and D. Li, *Appl. Catal. B*, 2012, **111**, 141-149.
53 T. Y. Ma, Y. Zheng, S. Dai, M. Jaroniec and S. Z. Qiao, *J. Mater. Chem. A*, 2014, **2**, 8676-8682.
54 H. M. Chen, P. K. Chu, J. H. He, T. Hu and M. Q. Yang, *J. colloid interface Sci.*, 2011, **359**, 68-8682.
55 W. Zhang, Z. Yang, X. Wang, Y. Zhang, X. Wen and S. Yang, *Catal. Commun.*, 2006, **7**, 408-412.
56 C. L. Yu, G. Li, L. F. Wei, Q. Z. Fan, Q. Shu and J. C. Yu, *Catalysis Today*, 2014, **224**, 154-162.

FULL PAPER

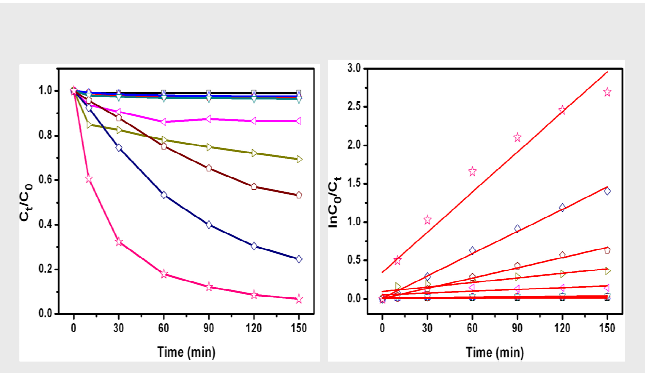

The as-prepared MnO_2, especially for the β-MnO_2, exhibits superior degradation ability compared to the conventional adsorbents.

Pan-Yong Kuang[a], Min-Hua Liang[a], Wan-Yi Kong[a], Zhao-Qing Liu[a,], Yun-Ping Guo[a], Hong-Juan Wang[a], Nan Li[a], Yu-Zhi Su[a], and Shuang Chen[b,*]*

Page No. – Page No.

Degradation rates of MB (100 mL, 20 mg/L on different adsorbents and corresponding plot of $\ln(C_0/C_t)$ versus degradation time.